

---

# Bridging Operator Learning and Conditioned Neural Fields: A Unifying Perspective

---

**Sifan Wang**\*

Graduate Program in Applied Mathematics  
and Computational Science  
University of Pennsylvania  
sifanw@sas.upenn.edu

**Jacob H. Seidman**\*

Graduate Program in Applied Mathematics  
and Computational Science  
University of Pennsylvania  
seidj@sas.upenn.edu

**Shyam Sankaran**

Department of Mechanical Engineering  
and Applied Mechanics  
University of Pennsylvania  
shyamss@seas.upenn.edu

**Hanwen Wang**

Graduate Program in Applied Mathematics  
and Computational Science  
University of Pennsylvania  
wangh19@sas.upenn.edu

**George J. Pappas**

Department of Electrical  
and Systems Engineering  
University of Pennsylvania  
pappasg@seas.upenn.edu

**Paris Perdikaris**

Department of Mechanical Engineering  
and Applied Mechanics  
University of Pennsylvania  
pgp@seas.upenn.edu

## Abstract

Operator learning is an emerging area of machine learning which aims to learn mappings between infinite dimensional function spaces. Here we uncover a connection between operator learning architectures and conditioned neural fields from computer vision, providing a unified perspective for examining differences between popular operator learning models. We find that many commonly used operator learning models can be viewed as neural fields with conditioning mechanisms restricted to point-wise and/or global information. Motivated by this, we propose the Continuous Vision Transformer (CViT), a novel neural operator architecture that employs a vision transformer encoder and uses cross-attention to modulate a base field constructed with a trainable grid-based positional encoding of query coordinates. Despite its simplicity, CViT achieves state-of-the-art results across challenging benchmarks in climate modeling and fluid dynamics. Our contributions can be viewed as a first step towards adapting advanced computer vision architectures for building more flexible and accurate machine learning models in physical sciences.

## 1 Introduction

Neural fields have recently gained prominence in computer vision as a memory-efficient approach for representing high-resolution images and scenes. At their core, neural fields are simply functions over a continuous domain that are parameterized by neural networks [1]. A key advance has been the development of conditioned neural fields, which allow these models to change based on auxiliary

---

\*These authors contributed equally.

<sup>1</sup>Our code is available at <https://github.com/PredictiveIntelligenceLab/cvit>

inputs. This is achieved through a base field combined with conditioning mechanisms that modulate the field’s forward pass to encode multiple signals into a single neural network architecture [2].

In parallel, the field of scientific machine learning has seen the emergence of neural operators – a class of deep learning models well-suited for operating on functional data common in physical sciences applications, such as building surrogates for expensive partial differential equation (PDE) solvers. For example, neural operators can learn mappings between infinite-dimensional function spaces to accelerate fluid dynamics simulations [3]. The formulation of widely used neural operator architectures like Fourier Neural Operators (FNO) [4, 5] and DeepONet [6, 7] is primarily motivated by mathematical intuition about the structure of the spaces that PDE solutions live in. These architectures are often supported by universal approximation guarantees [8, 9, 10, 11], ensuring their theoretical robustness. Furthermore, these models can also be interpreted as learning low-dimensional manifolds in function spaces [12, 13]. However, from a deep learning perspective, the architectural choices in current neural operator models appear quite distant to the wealth of techniques employed in other domains, potentially limiting their performance.

In this work, we uncover a previously unexplored connection between operator learning architectures and conditioned neural fields, providing a unifying framework to compare and contrast popular operator learning methods. Specifically, our main contributions can be summarized as follows:

- **Neural operators as conditioned neural fields.** We observe that many widely used operator learning models can be reformulated as neural fields with conditioning mechanisms restricted to pointwise and/or global information.
- **A unifying perspective.** We provide a general rubric for examining and contrasting neural operators through their respective choices of conditioning mechanisms and base fields.
- **Introducing the Continuous Vision Transformer (CViT).** We put forth a novel neural operator that employs a vision transformer encoder and cross-attention to modulate a base field built with a trainable grid-based positional encoding of query coordinates.
- **Simplicity meets state-of-the-art performance.** We demonstrate that, despite its simplicity, CViT achieves state-of-the-art performance on challenging benchmarks in climate modeling and fluid dynamics.

Taken together our results demonstrate the potential of adapting advanced computer vision architectures to develop more flexible and accurate machine learning models for physical sciences. Our contributions represent a rigorous initial step towards bridging the gap between the fields of computer vision and scientific machine learning, and aim to spark further research in this direction.

## 2 Neural Fields

A neural field is a function over a continuous domain parameterized by a neural network [1]. Recently, the computer vision community has adopted neural fields to represent 3D spatial fields, such as neural radiance fields (NeRFs) [14], spatial occupancy fields [15], and signed distance functions [16]. These fields represent functions defined over continuous spatial domains, with NeRFs additionally taking an element of a continuous ray space as input. In this paper, a point in the domain of a neural field is referred to as a *query point*, here denoted by  $y$ . Conditioned neural fields allow these fields to change based on auxiliary inputs  $u$ , often represented as latent codes  $z$ , without the need to retrain the entire field; see Figure 1. The latent code affects the forward pass by modifying the parameters of the base field through either global conditioning, where the forward pass is affected uniformly across all query points, or local conditioning, where the modifications depend on the specific query point.

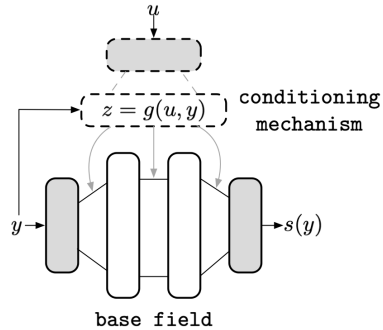


Figure 1: The structure of a *conditioned neural field* with both global and local conditioning.

**Global Conditioning.** Global conditioning in a neural field refers to modifying the forward pass only by the input  $u$  and in a uniform manner over the entire query domain. This can be achieved

through concatenation, where a global latent code is appended to the query vector and passed together through an MLP [17, 18, 19]. Alternatively, a hypernetwork could accept the auxiliary input and determine the neural field’s parameter values based on this input [20]. However, modifying every parameter of the base field for different auxiliary inputs can be computationally expensive. For example, feature-wise Linear Modulation (FiLM) [21], which originates from conditional batch normalization [22], has been proposed to modify only the sine activation function parameters in a SIREN network [23]. This technique has been used for global conditioning in methods such as  $\pi$ -GAN [24].

**Local Conditioning.** Local conditioning occurs when the latent code  $z$ , which modifies the base field’s parameters, is a function of the input query  $y$ , i.e.,  $z = g(y)$ . This results in query-dependent field parameters that can vary across the query domain. A common approach to generate local latent codes is to process the image or scene with a convolutional network and extract features from activations with receptive fields containing the query point. This can be done using 2D convolutions of projected 3D scenes [25, 26, 27] or 3D convolutions [28, 29, 30]. Muller *et al.* [31] learn features directly on multiresolution grid vertices and create local features via nearest grid point interpolation for each grid. Chan *et al.* [32] create features along three 2D planes and interpolate features from projections onto these planes. DeVries *et al.* [33] learn latent codes over patches on a 2D “floorplan” of a scene. Other methods divide the query domain into patches or voxels and learn a latent code  $z$  for each patch or voxel [34, 35, 36].

### 3 Operator Learning Architectures as Neural Fields

Here we demonstrate that many popular operator learning architectures are in fact neural fields with local and/or global conditioning. While connections between architectures such as the DeepONet and the Fourier Neural Operator have been described previously [10], they are typically formulated under certain architecture choices which allow these architectures to approximate one another. In contrast, here we show that, by viewing these architectures as conditioned neural fields, they are explicitly related through their respective choices of conditioning mechanisms and base fields.

#### 3.1 Encoder-Decoder Neural Operators

A large class of operator learning architectures can be described as encoder-decoder architectures according to the following construction. To learn an operator  $\mathcal{G} : \mathcal{X} \rightarrow \mathcal{Y}$ , an input function  $u \in \mathcal{X}$  are first mapped to a finite dimensional latent representation through the encoding map  $\mathcal{E} : \mathcal{X} \rightarrow \mathbb{R}^n$ . This latent representation is then mapped to a callable function through a decoding map  $\mathcal{D} : \mathbb{R}^n \rightarrow \mathcal{Y}$ . The composition of these two maps gives the architecture of the operator approximation scheme,  $\mathcal{G} = \mathcal{D} \circ \mathcal{E}$ . The class of encoder-decoder architectures includes the DeepONet [6], the PCA-based architecture of [37], and NoMaD [12].

These encoder-decoder architectures can be seen as neural fields with a global conditioning mechanism by viewing the role of the decoder as an operator which performs the conditioning of a base field, with a latent code derived from a parameterized encoder,  $z = \mathcal{E}_\phi(u)$ .

**DeepONet.** For example, in a DeepONet, the base field is a neural network  $t_\theta(y)$  (trunk network) appended with a last linear layer, and the decoder map conditions the weights of this last layer via the output of the encoding map  $\mathcal{E}_\phi(u)$  (branch network); see Figure 2(a) for a visual illustration. In other words, the decoder map is a weighted linear combination of  $n$  basis elements  $t_\theta(y)$ , where the weights are modulated by a global encoding of the input function  $\mathcal{E}_\phi(u)$ , yielding outputs of the form  $s(y) = \langle \mathcal{E}_\phi(u), t_\theta(y) \rangle$ . The PCA-based architecture of [37] can be viewed analogously using as basis elements the leading  $n$  eigenfunctions of the empirical covariance operator computed over the output functions in the training set.

**NoMaD.** Seidman *et al.* [12] demonstrated how encoder-decoder architectures can employ non-linear decoders to learn low-dimensional manifolds in an ambient function space. These so-called NoMaD architectures typically perform their conditioning by concatenating the input function encoding with the query input, i.e.,  $s(y) = f_\theta(y, \mathcal{E}_\phi(u))$ ; see Figure 2(b) for an illustration.

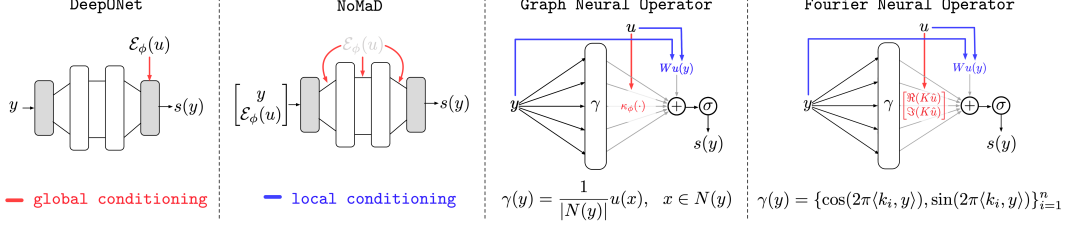


Figure 2: Viewing common neural operators as conditioned neural fields. Base field and conditioning mechanisms for: (a) DeepONet; (b) NoMaD; (c) the GNO layer; (d) the FNO layer.

### 3.2 Integral Kernel Neural Operators

Integral Kernel Neural Operators form another general class of neural operators that learn mappings between function spaces by approximating the integral kernel of an operator using neural networks. They were introduced as a generalization of the Neural Operator framework proposed by Li *et al.* [38]. The key idea behind here is to represent the operator  $\mathcal{G} : \mathcal{X} \rightarrow \mathcal{Y}$  as an integral kernel,  $\mathcal{G}(u)(y) = \int_{\Omega} \kappa(x, y, u(x))dx$ , where  $\kappa$  is a kernel function. In practice, the kernel function  $\kappa$  is parameterized by a neural network, and the integral is then approximated using a quadrature rule, such as Monte Carlo integration, Gaussian quadrature, or via spectral convolution in the frequency domain.

**Graph Neural Operator (GNO).** A single layer of the GNO [38] is given by

$$s(y) = \sigma\left(Wu(y) + \frac{1}{|N(y)|} \sum_{x \in N(y)} \kappa_{\phi}(x, y, u(x))u(x)\right), \quad (1)$$

where  $W \in \mathbb{R}^{d_u \times d_s}$  is a trainable weight matrix, and  $\kappa_{\phi}(\cdot)$  is a local message passing kernel parameterized by  $\phi$  [38]. As illustrated in Figure 2(c), the GNO layer is a conditioned neural field with local and global conditioning on the input function  $u$ . The base field uses a fixed positional encoding  $\gamma(y)$  that maps query coordinates  $y$  to input function values at neighboring nodes  $x \in N(y)$ , i.e.,  $\gamma(y) = u(x)/|N(y)|$ , followed by a linear layer. The encoding width equals the maximum number of neighboring nodes, with zeros filling trailing entries for queries with fewer neighbors. The GNO layer is conditioned globally via the parameterized kernel  $\kappa_{\phi}(\cdot)$  modulating the linear layer weights, and locally via a position-depended bias term  $Wu(y)$  added as a skip connection. The layer outputs  $s(y)$  are finally obtained by summing the linear layer outputs and the skip connection, then applying a nonlinear activation function  $\sigma$ .

**Fourier Neural Operator (FNO).** The FNO introduced a computationally efficient approach for performing global message passing in GNO layers assuming a stationary kernel  $\kappa_{\phi}(\cdot)$  [4, 39]. Leveraging the Fourier transform, a single layer of FNO [4] is given by

$$s(y) = \sigma\left(Wu(y) + \mathcal{F}_n^{-1}(K\mathcal{F}_n(u))(y)\right), \quad (2)$$

where  $W \in \mathbb{R}^{d_o \times d_o}$  and  $K \in \mathbb{R}^{n \times n}$  are trainable weight matrices,  $\mathcal{F}_n : L^2 \rightarrow \mathbb{C}^n$  is the Fourier transform truncated to the first  $n$  modes, and  $\mathcal{F}_n^{-1} : \mathbb{C}^n \rightarrow L^2$  is the left inverse of this operator. We show that the FNO layer can be viewed as a conditioned neural field employing both local and global conditioning on the input function  $u$ . Without loss of generality, we demonstrate this for a one-dimensional query domain  $y \in \mathbb{R}$ . To this end, note that the convolutional part of the FNO layer (equation 2) can be re-written as (see Appendix B for a derivation)

$$\mathcal{F}_n^{-1}(K\mathcal{F}_n(u))(y) = \sum_{j=1}^n \Re(K\hat{u})_j \cos(2\pi\langle k_j, y \rangle) - \sum_{j=1}^n \Im(K\hat{u})_j \sin(2\pi\langle k_j, y \rangle), \quad (3)$$

where  $\hat{u} = \mathcal{F}_n u$  denotes the truncated Fourier transform of  $u$ , and  $\Re(z)$  and  $\Im(z)$  denote the real and imaginary parts of a complex vector  $z \in \mathbb{C}^n$ . We may interpret this transformation of  $u(y)$  as a linear transformation (which depends on  $\hat{u}$ ) acting on the positional encoding,

$$\gamma(y) = [\cos(2\pi\langle k_1, y \rangle), \sin(2\pi\langle k_1, y \rangle), \dots, \cos(2\pi\langle k_n, y \rangle), \sin(2\pi\langle k_n, y \rangle)]^T. \quad (4)$$

The resulting expression (equation 3) is then acted on with a position dependant bias term  $Wu(y)$ , followed by a pointwise nonlinearity  $\sigma$ . In this manner, we see that an FNO layer is a neural field with a fixed positional encoding (first  $n$  Fourier features), a global conditioning of the weights by the Fourier transform of  $u$ , and a local conditioning acting as a bias term by  $Wu(y)$ ; see Figure 2(d) for an illustration. This neural field interpretation also suggests an alternative way for implementing FNO layers by explicitly using equation 3 to compute the inverse Fourier transform, thereby allowing them to be evaluated at arbitrary query points instead of a fixed regular grid.

**Extending to other neural operators.** In practice, GNO and FNO layers are stacked to form deeper architectures with a compositional structure. These can also be interpreted as conditioned neural fields, where the base field corresponds to the last GNO or FNO layer, while all previous layers are absorbed into the definition of the conditioning mechanism. Analogously, one can examine a broader collection of models that fall under the class of Integral Kernel Neural Operators, such as [40, 41, 42, 43, 44].

## 4 Continuous Vision Transformer (CViT)

While the mathematical foundations of neural operators are well-established [8, 9, 10, 11], the architectural design of these models has not kept pace with the rapid advancements in deep learning. As shown in the previous section, the most common neural operator architectures, such as GNO, FNO, DeepONet, and NoMaD, essentially rely on simple building blocks like Fourier layers or fully connected networks, which may not effectively capture the complex spatial dependencies and multiscale features present in many physical systems. In contrast, computer vision has seen a proliferation of sophisticated architectures, such as convolutional neural networks and vision transformers, which have been highly successful in learning rich representations from complex high-dimensional data. This suggests that there is significant potential to improve the performance and expressiveness of neural operators by drawing inspiration from these advanced techniques.

By using the perspective of neural fields as a bridge to these computer vision architectures, we introduce the Continuous Vision Transformer (CViT), a novel neural operator architecture that combines the strengths of vision transformers and neural fields to learn more powerful and flexible representations of time-dependent physical systems. The CViT can be viewed as a well-defined conditioned neural field with transformer architectures being the base field and conditioning function. As we will see in detail in the following paragraphs, the base field comprises of a trainable positional encoding of query coordinates (see equation 5), followed by a standard Transformer decoder. This base field transformer is then globally conditioned by cross-attention, using the output of a standard ViT backbone as key and values, which is evaluated on the input function  $u$ . See Figure 3 for a visual summary.

**Base field of CViT.** The base field of CViT consists of three components: a positional embedding, a transformer backbone, and a nonlinear projection mapping. To create the positional encoding, we start by creating a uniform grid  $\{\mathbf{y}_{ij}\} \subset [0, 1]^2$ , for  $i = 1, \dots, N_x$  and  $j = 1, \dots, N_y$ , along with associated trainable latent grid features  $\mathbf{x} \in \mathbb{R}^{N_x \times N_y \times C}$  [28, 45, 46]. Here  $\mathbf{x}$  is initialized by a unit Gaussian distribution, and the hyper-parameters  $N_x, N_y$  are typically set to match the resolution of the target output functions. For a single arbitrary query point  $y \in \mathbb{R}^2$ , we then compute a Nadaraya-Watson interpolant [47, 48] over grid latent features  $\mathbf{x}$  as follows,

$$\mathbf{x}' = \sum_{i=1}^{N_x} \sum_{j=1}^{N_y} w_{ij} \mathbf{x}_{ij}, \quad w_{ij} = \frac{\exp(-\epsilon \|y - \mathbf{y}_{ij}\|^2)}{\sum_{ij} \exp(-\epsilon \|y - \mathbf{y}_{ij}\|^2)}, \quad (5)$$

where  $\epsilon > 0$  is a hyper-parameter that determines the locality of the interpolated features. The positional encoding from the interpolated grid feature  $\mathbf{x}_0 = \mathbf{x}' \in \mathbb{R}^{1 \times C}$  is then fed as query inputs to the transformer backbone, where we globally condition its output with a latent variable  $\mathbf{z}_L(u)$  of the input  $u$  (to be described next) as keys and values, applying  $K$  cross-attention Transformer blocks as

$$\begin{aligned} \mathbf{x}'_k &= \mathbf{x}_{k-1} + \text{MHA}(\text{LN}(\mathbf{x}_{k-1}), \text{LN}(\mathbf{z}_L), \text{LN}(\mathbf{z}_L)), & k &= 1 \dots K, \\ \mathbf{x}_k &= \mathbf{x}'_k + \text{MLP}(\text{LN}(\mathbf{x}'_k)), & k &= 1 \dots K. \end{aligned}$$

Finally, we use a small MLP network to project the output of the transformer backbone to the desired dimension.

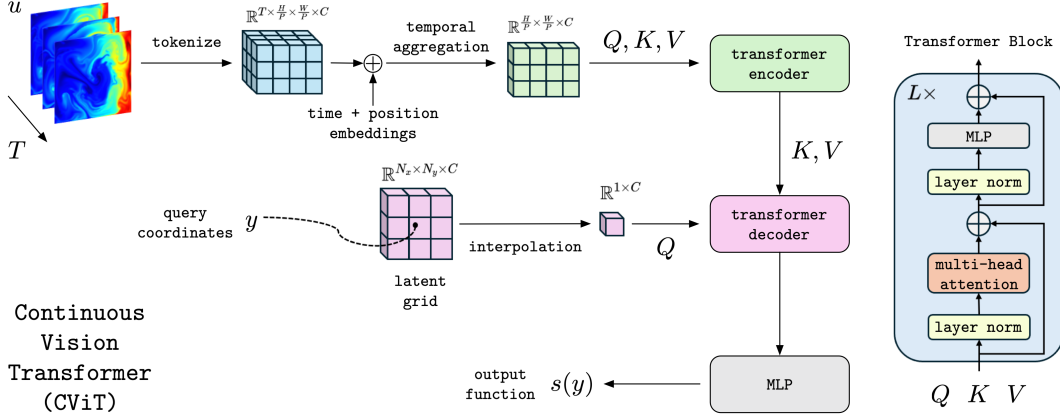


Figure 3: *Continuous Vision Transformer (CViT)*: CViT builds a base field that consists of a trainable grid-based positional encoding of query coordinates  $y$ , followed by a standard transformer decoder [50]. The keys and values vectors of the base field are modulated via a global conditioning on the input function  $u$ , which is encoded by a vision transformer backbone.

**Conditioning function of CViT.** The conditioning function takes the input function  $u$  as an input and returns the latent conditioning variable  $z_L$ . We first construct a gridded representation of the input function  $u$  yielding a 2+1 dimensional spatio-temporal data tensor  $\mathbf{u} \in \mathbb{R}^{T \times H \times W \times D}$  with  $D$  channels. We patchify our inputs into 3D tokens  $\mathbf{u}_p \in \mathbb{R}^{T \times \frac{H}{P} \times \frac{W}{P} \times C}$  by tokenizing each 2D spatial frame independently using the same patch embedding process as in standard ViTs [49]. We then add (with broadcasting) trainable 1D temporal and 2D spatial positional embeddings to each token using broadcasting, as shown below:

$$\mathbf{u}_{pe} = \mathbf{u}_p + \text{PE}_t + \text{PE}_s, \quad \text{PE}_t \in \mathbb{R}^{T \times 1 \times 1 \times C}, \quad \text{PE}_s \in \mathbb{R}^{1 \times \frac{H}{P} \times \frac{W}{P} \times C}.$$

Next, we use a temporal aggregation layer to reduce the token sequence length, and thereby the computational cost of subsequent self-attention layers [50]. This aggregation is performed using the Perceiver architecture put forth by Jaegle *et al.* [51]. Specifically, we learn a predefined number of latent input queries  $\mathbf{z} \in \mathbb{R}^{1 \times C}$  by applying a cross-attention module that maps the flattened visual features  $\mathbf{u}_f \in \mathbb{R}^{(\frac{H}{P} \times \frac{W}{P}) \times T \times C}$  to a latent tensor  $\mathbf{z}_{agg} \in \mathbb{R}^{(\frac{H}{P} \times \frac{W}{P}) \times 1 \times C}$  as

$$\begin{aligned} \mathbf{z}' &= \hat{\mathbf{z}} + \text{MHA}(\text{LN}(\hat{\mathbf{z}}), \text{LN}(\mathbf{u}_f), \text{LN}(\mathbf{u}_f)), \\ \mathbf{z}_{agg} &= \mathbf{z}' + \text{MLP}(\text{LN}(\mathbf{z}')), \end{aligned}$$

where  $\mathbf{z}$  is trainable and initialized by a unit Gaussian distribution, and  $\hat{\mathbf{z}} \in \mathbb{R}^{(\frac{H}{P} \times \frac{W}{P}) \times 1 \times C}$  is obtained by tiling the latent query  $\mathbf{z}$   $(\frac{H}{P} \times \frac{W}{P})$  times. We then process the aggregated tokens  $\mathbf{z}_{agg}$  using a sequence of  $L$  pre-norm Transformer blocks [50, 52],

$$\begin{aligned} \mathbf{z}_0 &= \mathbf{z}_{agg}, \\ \mathbf{z}'_\ell &= \text{MSA}(\text{LN}(\mathbf{z}_{\ell-1})) + \mathbf{z}_{\ell-1}, & \ell &= 1 \dots L \\ \mathbf{z}_\ell &= \text{MLP}(\text{LN}(\mathbf{z}'_\ell)) + \mathbf{z}'_\ell, & \ell &= 1 \dots L. \end{aligned}$$

**Comparison to other transformer-based methods.** Here it is important to emphasize that the CViT base field performs cross-attention between each individual query point and the output tokens of the conditioning function. This is a subtle but significant difference from prior work, such as Oformer [53] and GNOT [54], where model predictions from different query locations are correlated because cross-attentions are computed for all queries simultaneously. In contrast, CViT vectorizes the cross-attention module across query coordinates via `vmap` in JAX [55]. Consequently, the model predictions corresponding to different query coordinates are independent of each other, thereby allowing us to build a well-defined conditioned neural field.

## 5 Experiments

We compare the CViT against popular neural operators on three challenging benchmarks in physical sciences. In addition to demonstrating CViT’s performance against strong baselines, we also conduct comprehensive ablation studies to probe the sensitivity on its own hyper-parameters.

**CViT model setup.** We construct CViT models with different configurations, as summarized in Appendix Table 4. For all experiments, unless otherwise stated, we use a patch size of  $8 \times 8$  for tokenizing inputs. We also employ a base field with a single cross-attention Transformer block for all configurations. While we tested base fields with multiple layers, they did not yield improvements. The grid resolution is set to the spatial resolution of each dataset. The latent dimension of grid features is set to 512, and if it does not match the transformer’s embedding dimension, we align it using a dense layer. Besides, we use  $\epsilon = 10^5$  to ensure sufficient locality of the interpolated features. These choices are validated by extensive ablation studies, as illustrated in Figure 6. Full details of the training and evaluation procedures are provided in Appendix C.1.

**Baselines.** We select the following methods as our baselines for comparisons. **DeepONet** [6]: One of the first neural operators with universal approximation guarantees. **NoMaD** [12]: A recently proposed architecture leveraging nonlinear decoders to achieve enhanced dimensionality reduction. **FNO** [4]: An efficient framework for operator learning in the frequency domain. **FFNO** [5]: An improved version of FNO utilizing a separable Fourier representation, which reduces model complexity and facilitates deeper network structures. **UNO** [56]: A U-shaped neural operator with FNO layers. **U-Net<sub>att</sub>** [57]: A modern U-Net architecture using bias weights and group normalization, and wide ResNet-style 2D convolutional blocks, each of which is followed by a spatial attention block. **U-F2Net** [57]: A U-Net variant where the lower blocks in both the downsampling and upsampling paths are replaced by Fourier blocks, each consisting of 2 FNO layers with residual connections. **Dilated ResNet** [58]: A ResNet model that adapts filter sizes at different layers using dilated convolutions, providing an alternative method for aggregating global information. **GK-Transformer** [59] / **OFormer** [53] / **GNOT** [54]: Various transformer-based architectures for operator learning, with different designs of their encoder/decoder and attention mechanisms. **DPOT** [60]: Another transformer-based network with a Fourier attention layer, pre-trained on extensive PDE datasets using an auto-regressive denoising strategy.

For all baselines, we report evaluation results from the original papers when applicable. When not applicable, we train and evaluate each model following the suggested settings in the respective paper. Details on the implementation of baseline models are provided in Appendix C.2.

### 5.1 Main Results

Here we provide our main results across three challenged benchmarks. The full details on the underlying equations, dataset generation and problem setup for each case are provided in the Appendix; see Section C.3, C.4 and C.5, respectively.

**Advection of discontinuous waveforms.** The first benchmark involves predicting the transport of discontinuous waveforms governed by a linear advection equation with periodic boundary conditions. We make use of the datasets and problem setup established by Hoop *et al.* [61]. This benchmark evaluates our model’s capability in handling discontinuous solutions and shocks in comparison to popular neural operator models.

Figure 4 illustrates the test sample corresponding to the worst-case prediction of each model we compared. We observe that CViT is able to better capture the discontinuous targets and yield the most sharp predictions across all baselines. This is also reflected in both the relative L2 and Total Variation error metrics; see Appendix Table 5 for a more complete summary, including details on model configurations, as well as average, median and worst case errors across the entire test dataset.

**Shallow-water equations.** The second benchmark involves a fluid flow system governed by the 2D shallow-water equations. This describes the evolution of a 2D incompressible flow on the surface of the sphere and it is commonly used as a benchmark in climate modeling. Here we adhere to the dataset and problem setup established in PDEArena [57], allowing us to perform fair comparisons with several state-of-the-art deep learning surrogates.

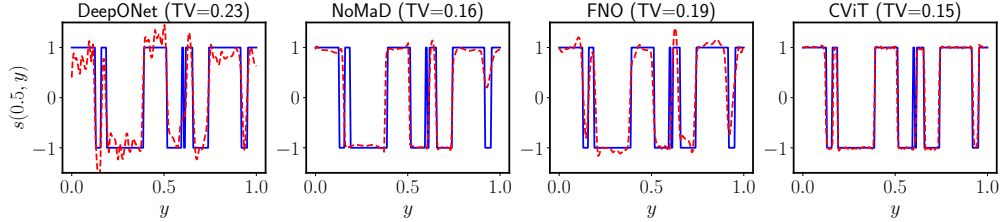


Figure 4: *Advection of discontinuous waveforms*. Prediction (red dashed line) versus ground truth (blue line) for the worst-case example in the test dataset, for: DeepONet; NoMaD; FNO; CViT. Also reported is the associated Total Variation (TV) error ( $\downarrow$ ).

Table 1: Performance for 5-step roll-out predictions in the shallow-water equations benchmark (at resolution  $96 \times 192$  for both training and testing).

Model	# Params	Rel. $L^2$ error ( $\downarrow$ )
DilResNet	4.2 M	13.20%
U-Net <sub>att</sub>	148 M	5.684%
FNO	268 M	3.97 %
U-F2Net	344 M	1.89 %
UNO	440 M	3.79%
<b>CViT-S</b>	13 M	<b>4.47 %</b>
<b>CViT-B</b>	30 M	<b>2.69 %</b>
<b>CViT-L</b>	92 M	<b>1.56 %</b>

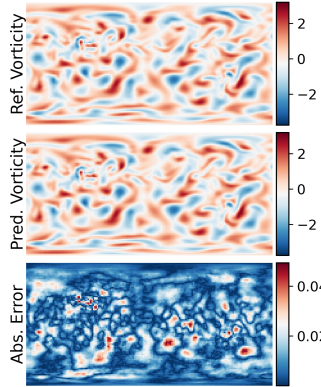


Figure 5: *Shallow-water equations benchmark*: Representative CViT prediction of the vorticity field at 48hr lead time, and point-wise error versus the ground truth.

Table 1 presents the results of CViT against several competitive and heavily optimized baselines. Our proposed method achieves the lowest relative  $L^2$  error. It is also worth noting that the reported performance gains are achieved using CViT configurations with a significantly smaller parameter count compared to the other baselines. This highlights the merits of our neural fields approach that enables the design of parameter-efficient models whose outputs can also be continuously queried at any resolution. Additional visualizations of our models are shown in Figure 9 and 10.

In addition, here we perform extensive ablation studies on the hyper-parameters of CViT. The results are summarized in Figure 6. We observe that a smaller patch size typically leads to better accuracy, but at higher computational cost. Moreover, model performance is significantly influenced by the type of coordinate embeddings used in the CViT base field. In order to ablate this choice, we consider two additional approaches to constructing these embeddings: (a) a small MLP, and (b) random Fourier features [62]. Our experiments reveal that the proposed grid-based embedding achieves the best accuracy, outperforming other methods by up to an order of magnitude. We also investigate the impact of the resolution of the associated grid. Our findings suggest that best results are obtained when the grid resolution matches the highest resolution at which the model is evaluated. Additionally, the CViT model shows sensitivity to the hyper-parameter  $\epsilon$  used for computing interpolated features; too small  $\epsilon$  values can degrade predictive accuracy. Finally, while we observe minor improvements by increasing the latent dimension of grid features, or the number of base field attention heads, the overall model performance remains robust to variations in these hyper-parameters; see Appendix Figure 8.

**Navier-Stokes equations.** Our last benchmark corresponds to predicting the evolution of a 2D buoyancy-driven flow, depicting a smoke volume rising in a bounded square domain. The underlying governing equations are the incompressible Navier-Stokes equations coupled with a passive scalar transport equation. For a fair comparison with various neural operators and other state-of-the-art



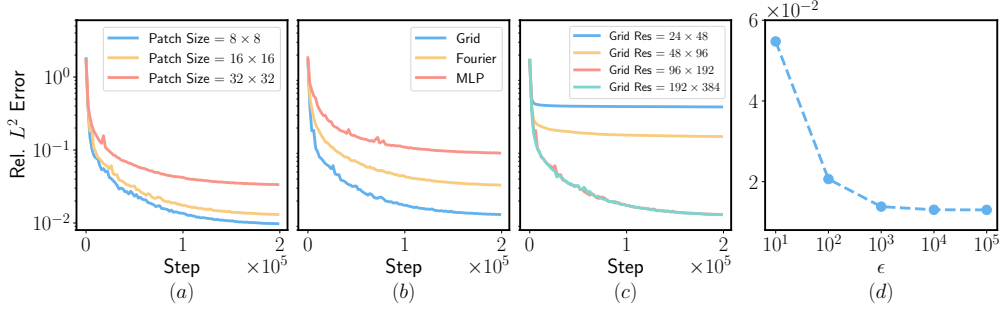


Figure 6: *Ablation studies for CViT on the shallow-water equations benchmark.* Convergence of test errors for: (a) different patch sizes; (b) different coordinate embeddings; (c) different resolutions of latent grids; (d) sensitivity on interpolating the CViT latent grid features, as controlled by the  $\epsilon$  parameter. Results obtained using CViT-L with  $16 \times 16$  patch-size, varying each hyper-parameter of interest while keeping others fixed.

Table 2: Performance on the Navier-Stokes benchmark. All mode ( $128 \times 128$  resolution for both training and testing).

Model	# Params	Rel. $L^2$ error ( $\downarrow$ )
FNO	0.5 M	9.12 %
FFNO	1.3 M	8.39 %
GK-T	1.6 M	9.52%
GNOT	1.8 M	17.20 %
Oformer	1.9 M	13.50 %
DPOT-Ti	7 M	12.50 %
DPOT-S	30 M	9.91 %
DPOT-L (Pre-trained)	500 M	7.98 %
DPOT-L (Fine-tuned)	500 M	2.78 %
DPOT-H (Pre-trained)	1.03 B	3.79 %
<b>CViT-S</b>	13 M	<b>3.75 %</b>
<b>CViT-B</b>	30 M	<b>3.18 %</b>
<b>CViT-L</b>	92 M	<b>2.35 %</b>

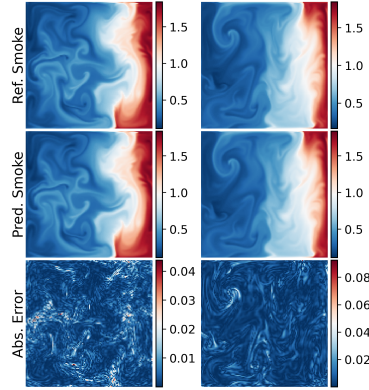


Figure 7: *Navier-Stokes benchmark.* Representative CViT predictions of the passive scalar field, and point-wise error against the ground truth.

deep learning models, we use the dataset generated by PDEArena [57], and follow the problem setup reported in Hao *et al.* [60].

Our main results are summarized in Table 2, indicating that CViT outperforms all baselines we have considered. Notably, the previous best result (DPOT-L (Fine-tuned)) is achieved with a much larger transformer-based architecture, which involves pretraining on massive diverse PDE datasets followed by fine-tuning on the target dataset for 500 epochs. Furthermore, CViT exhibits remarkable parameter efficiency. CViT-small, with only 13M parameters, achieves accuracy comparable to the largest pretrained model (1.03B). Additionally, CViT shows good scalability; as the number of parameters increases, performance improves. These findings strongly support the effectiveness of our approach in learning evolution operators for complex physical systems. Additional results and sample visualizations are provided in Figure 7, as well as Figure 11, 12 and 13 in the Appendix.

## 6 Discussion

**Summary.** This work uncovers a novel connection between operator learning architectures and conditioned neural fields from computer vision. By reformulating popular operator learning models as neural fields with specific conditioning mechanisms, we provide a unifying perspective for understanding and comparing these architectures. Motivated by these findings, we introduce the Continuous Vision Transformer (CViT), a new operator learning architecture that leverages the power of vision transformers and cross-attention to modulate a transformer base field, achieving state-of-the-

art accuracy on challenging benchmarks in climate modeling and fluid dynamics. These contributions demonstrate the potential of adapting advanced computer vision techniques to develop more flexible and accurate machine learning models for physical sciences, bridging the gap between the two fields and paving the way for further research in this direction. The broader impact of this work lies in its potential to fuel the development of resolution-invariant foundation models for accelerating scientific discovery and enable more efficient and accurate simulations of complex physical systems, with applications ranging from climate modeling to engineering design.

**Limitations.** Despite its promising performance, the proposed CViT architecture faces several limitations and open challenges. Firstly, like most transformer-based models, CViT’s self-attention blocks scale quadratically with the number of tokens, posing computational challenges for high-dimensional or high-resolution data. Recent advancements in computer vision [63] are tackling these scalability issues, and these ideas can be transferred to our setting. Secondly, transformer-based models like CViT require large training datasets for optimal performance, and may struggle in data-scarce scenarios without careful regularization. Leveraging CViT’s ability to reconstruct continuous output functions, physics-informed loss functions [64, 65] can be used for data-efficient training and regularization. Lastly, while the experiments presented here treat input functions as a sequence of images, many practical applications involve complex geometric structures and diverse input modalities like meshes and point clouds. Addressing these cases requires developing appropriate tokenization schemes, and recent work in [66, 67] has taken steps in this direction.

**Potential Negative Societal Impacts.** Our contributions enables advances in accelerating the modeling and emulation of physical systems. As with any tool that furthers our understanding and ability to predict the outcomes of complex systems, there may be ill-intentioned use cases, but we do not expect any specific negative impact from this work.

## Acknowledgement

We would like to acknowledge support from the US Department of Energy under the Advanced Scientific Computing Research program (grant DE-SC0024563). We also thank the developers of the software that enabled our research, including JAX [55], Matplotlib [68], and NumPy [69].

## References

- [1] Kenneth O Stanley. Compositional pattern producing networks: A novel abstraction of development. *Genetic programming and evolvable machines*, 8:131–162, 2007.
- [2] Yiheng Xie, Towaki Takikawa, Shunsuke Saito, Or Litany, Shiqin Yan, Numair Khan, Federico Tombari, James Tompkin, Vincent Sitzmann, and Srinath Sridhar. Neural fields in visual computing and beyond. In *Computer Graphics Forum*, volume 41, pages 641–676. Wiley Online Library, 2022.
- [3] Kamyar Azizzadenesheli, Nikola Kovachki, Zongyi Li, Miguel Liu-Schiaffini, Jean Kossaifi, and Anima Anandkumar. Neural operators for accelerating scientific simulations and design. *Nature Reviews Physics*, pages 1–9, 2024.
- [4] Zongyi Li, Nikola Borislavov Kovachki, Kamyar Azizzadenesheli, Burigede liu, Kaushik Bhattacharya, Andrew Stuart, and Anima Anandkumar. Fourier neural operator for parametric partial differential equations. In *International Conference on Learning Representations*, 2021.
- [5] Alasdair Tran, Alexander Mathews, Lexing Xie, and Cheng Soon Ong. Factorized fourier neural operators. *arXiv preprint arXiv:2111.13802*, 2021.
- [6] Lu Lu, Pengzhan Jin, Guofei Pang, Zhongqiang Zhang, and George Em Karniadakis. Learning nonlinear operators via DeepONet based on the universal approximation theorem of operators. *Nature Machine Intelligence*, 3(3):218–229, 2021.
- [7] Sifan Wang, Hanwen Wang, and Paris Perdikaris. Improved architectures and training algorithms for deep operator networks. *Journal of Scientific Computing*, 92(2):35, 2022.
- [8] Tianping Chen and Hong Chen. Universal approximation to nonlinear operators by neural networks with arbitrary activation functions and its application to dynamical systems. *IEEE transactions on neural networks*, 6(4):911–917, 1995.

- [9] Samuel Lanthaler, Siddhartha Mishra, and George E Karniadakis. Error estimates for deepnets: A deep learning framework in infinite dimensions. *Transactions of Mathematics and Its Applications*, 6(1):tnac001, 2022.
- [10] Nikola Kovachki, Samuel Lanthaler, and Siddhartha Mishra. On universal approximation and error bounds for fourier neural operators. *Journal of Machine Learning Research*, 22:Art–No, 2021.
- [11] Tim De Ryck and Siddhartha Mishra. Generic bounds on the approximation error for physics-informed (and) operator learning. *Advances in Neural Information Processing Systems*, 35:10945–10958, 2022.
- [12] Jacob H Seidman, Georgios Kissas, Paris Perdikaris, and George J. Pappas. NOMAD: Nonlinear manifold decoders for operator learning. In Alice H. Oh, Alekh Agarwal, Danielle Belgrave, and Kyunghyun Cho, editors, *Advances in Neural Information Processing Systems*, 2022.
- [13] Jacob H Seidman, Georgios Kissas, George J. Pappas, and Paris Perdikaris. Variational autoencoding neural operators. In *Proceedings of the 40th International Conference on Machine Learning*, volume 202 of *Proceedings of Machine Learning Research*, pages 30491–30522. PMLR, 23–29 Jul 2023.
- [14] Ben Mildenhall, Pratul P Srinivasan, Matthew Tancik, Jonathan T Barron, Ravi Ramamoorthi, and Ren Ng. Nerf: Representing scenes as neural radiance fields for view synthesis. *Communications of the ACM*, 65(1):99–106, 2021.
- [15] Lars Mescheder, Michael Oechsle, Michael Niemeyer, Sebastian Nowozin, and Andreas Geiger. Occupancy networks: Learning 3d reconstruction in function space. In *Proceedings of the IEEE/CVF conference on computer vision and pattern recognition*, pages 4460–4470, 2019.
- [16] Jeong Joon Park, Peter Florence, Julian Straub, Richard Newcombe, and Steven Lovegrove. DeepSDF: Learning continuous signed distance functions for shape representation. In *Proceedings of the IEEE/CVF conference on computer vision and pattern recognition*, pages 165–174, 2019.
- [17] Zhiqin Chen and Hao Zhang. Learning implicit fields for generative shape modeling. In *Proceedings of the IEEE/CVF Conference on Computer Vision and Pattern Recognition*, pages 5939–5948, 2019.
- [18] Steven Liu, Xiuming Zhang, Zhoutong Zhang, Richard Zhang, Jun-Yan Zhu, and Bryan Russell. Editing conditional radiance fields. In *Proceedings of the IEEE/CVF International Conference on Computer Vision*, pages 5773–5783, 2021.
- [19] Wonbong Jang and Lourdes Agapito. Codenerf: Disentangled neural radiance fields for object categories. In *Proceedings of the IEEE/CVF International Conference on Computer Vision*, pages 12949–12958, 2021.
- [20] David Ha, Andrew M. Dai, and Quoc V. Le. Hypernetworks. In *International Conference on Learning Representations*, 2017.
- [21] Ethan Perez, Florian Strub, Harm De Vries, Vincent Dumoulin, and Aaron Courville. Film: Visual reasoning with a general conditioning layer. In *Proceedings of the AAAI Conference on Artificial Intelligence*, volume 32, 2018.
- [22] Harm De Vries, Florian Strub, Jérémie Mary, Hugo Larochelle, Olivier Pietquin, and Aaron C Courville. Modulating early visual processing by language. *Advances in Neural Information Processing Systems*, 30, 2017.
- [23] Vincent Sitzmann, Julien Martel, Alexander Bergman, David Lindell, and Gordon Wetzstein. Implicit neural representations with periodic activation functions. *Advances in Neural Information Processing Systems*, 33:7462–7473, 2020.
- [24] Eric R Chan, Marco Monteiro, Petr Kellnhofer, Jiajun Wu, and Gordon Wetzstein. pi-gan: Periodic implicit generative adversarial networks for 3d-aware image synthesis. In *Proceedings of the IEEE/CVF conference on computer vision and pattern recognition*, pages 5799–5809, 2021.
- [25] Qiangeng Xu, Weiyue Wang, Duygu Ceylan, Radomir Mech, and Ulrich Neumann. Disn: Deep implicit surface network for high-quality single-view 3d reconstruction. *Advances in neural information processing systems*, 32, 2019.

- [26] Alex Yu, Vickie Ye, Matthew Tancik, and Angjoo Kanazawa. pixelnerf: Neural radiance fields from one or few images. In *Proceedings of the IEEE/CVF Conference on Computer Vision and Pattern Recognition*, pages 4578–4587, 2021.
- [27] Alex Trevithick and Bo Yang. Grf: Learning a general radiance field for 3d representation and rendering. In *Proceedings of the IEEE/CVF International Conference on Computer Vision*, pages 15182–15192, 2021.
- [28] Songyou Peng, Michael Niemeyer, Lars Mescheder, Marc Pollefeys, and Andreas Geiger. Convolutional occupancy networks. In *Computer Vision–ECCV 2020: 16th European Conference, Glasgow, UK, August 23–28, 2020, Proceedings, Part III 16*, pages 523–540. Springer, 2020.
- [29] Lingjie Liu, Jiatao Gu, Kyaw Zaw Lin, Tat-Seng Chua, and Christian Theobalt. Neural sparse voxel fields. *Advances in Neural Information Processing Systems*, 33:15651–15663, 2020.
- [30] Julian Chibane, Thiemo Alldieck, and Gerard Pons-Moll. Implicit functions in feature space for 3d shape reconstruction and completion. In *Proceedings of the IEEE/CVF conference on computer vision and pattern recognition*, pages 6970–6981, 2020.
- [31] Thomas Müller, Alex Evans, Christoph Schied, and Alexander Keller. Instant neural graphics primitives with a multiresolution hash encoding. *ACM Transactions on Graphics (ToG)*, 41(4):1–15, 2022.
- [32] Eric R Chan, Connor Z Lin, Matthew A Chan, Koki Nagano, Boxiao Pan, Shalini De Mello, Orazio Gallo, Leonidas J Guibas, Jonathan Tremblay, Sameh Khamis, et al. Efficient geometry-aware 3d generative adversarial networks. In *Proceedings of the IEEE/CVF Conference on Computer Vision and Pattern Recognition*, pages 16123–16133, 2022.
- [33] Terrance DeVries, Miguel Angel Bautista, Nitish Srivastava, Graham W Taylor, and Joshua M Susskind. Unconstrained scene generation with locally conditioned radiance fields. In *Proceedings of the IEEE/CVF International Conference on Computer Vision*, pages 14304–14313, 2021.
- [34] Rohan Chabra, Jan E Lenssen, Eddy Ilg, Tanner Schmidt, Julian Straub, Steven Lovegrove, and Richard Newcombe. Deep local shapes: Learning local sdf priors for detailed 3d reconstruction. In *Computer Vision–ECCV 2020: 16th European Conference, Glasgow, UK, August 23–28, 2020, Proceedings, Part XXIX 16*, pages 608–625. Springer, 2020.
- [35] Edgar Tretschk, Ayush Tewari, Vladislav Golyanik, Michael Zollhöfer, Carsten Stoll, and Christian Theobalt. Patchnets: Patch-based generalizable deep implicit 3d shape representations. In *Computer Vision–ECCV 2020: 16th European Conference, Glasgow, UK, August 23–28, 2020, Proceedings, Part XVI 16*, pages 293–309. Springer, 2020.
- [36] Anpei Chen, Zexiang Xu, Andreas Geiger, Jingyi Yu, and Hao Su. Tensorf: Tensorial radiance fields. In *Computer Vision–ECCV 2022: 17th European Conference, Tel Aviv, Israel, October 23–27, 2022, Proceedings, Part XXXII*, pages 333–350. Springer, 2022.
- [37] Kaushik Bhattacharya, Bamdad Hosseini, Nikola B Kovachki, and Andrew M Stuart. Model reduction and neural networks for parametric PDEs. *The SMAI journal of computational mathematics*, 7:121–157, 2021.
- [38] Zongyi Li, Nikola Kovachki, Kamyar Azizzadenesheli, Burigede Liu, Kaushik Bhattacharya, Andrew Stuart, and Anima Anandkumar. Neural operator: Graph kernel network for partial differential equations. *arXiv preprint arXiv:2003.03485*, 2020.
- [39] J Bruna, W Zaremba, A Szlam, and Y LeCun. Spectral networks and deep locally connected networks on graphs. *arxiv. arXiv preprint arXiv:1312.6203*, 2014.
- [40] Gaurav Gupta, Xiongye Xiao, and Paul Bogdan. Multiwavelet-based operator learning for differential equations. *Advances in neural information processing systems*, 34:24048–24062, 2021.
- [41] Tapas Tripura and Souvik Chakraborty. Wavelet neural operator: a neural operator for parametric partial differential equations. *arXiv preprint arXiv:2205.02191*, 2022.
- [42] Qianying Cao, Somdatta Goswami, and George Em Karniadakis. Lno: Laplace neural operator for solving differential equations. *arXiv preprint arXiv:2303.10528*, 2023.
- [43] VS Fanaskov and Ivan V Oseledets. Spectral neural operators. In *Doklady Mathematics*, volume 108, pages S226–S232. Springer, 2023.

- [44] Miguel Liu-Schiaffini, Julius Berner, Boris Bonev, Thorsten Kurth, Kamyar Azizzadenesheli, and Anima Anandkumar. Neural operators with localized integral and differential kernels. *arXiv preprint arXiv:2402.16845*, 2024.
- [45] Chiyu Jiang, Avneesh Sud, Ameesh Makadia, Jingwei Huang, Matthias Nießner, Thomas Funkhouser, et al. Local implicit grid representations for 3d scenes. In *Proceedings of the IEEE/CVF Conference on Computer Vision and Pattern Recognition*, pages 6001–6010, 2020.
- [46] Ishit Mehta, Michaël Gharbi, Connelly Barnes, Eli Shechtman, Ravi Ramamoorthi, and Manmohan Chandraker. Modulated periodic activations for generalizable local functional representations. In *Proceedings of the IEEE/CVF International Conference on Computer Vision*, pages 14214–14223, 2021.
- [47] Elizbar A Nadaraya. On estimating regression. *Theory of Probability & Its Applications*, 9(1):141–142, 1964.
- [48] Geoffrey S Watson. Smooth regression analysis. *Sankhyā: The Indian Journal of Statistics, Series A*, pages 359–372, 1964.
- [49] Alexey Dosovitskiy, Lucas Beyer, Alexander Kolesnikov, Dirk Weissenborn, Xiaohua Zhai, Thomas Unterthiner, Mostafa Dehghani, Matthias Minderer, Georg Heigold, Sylvain Gelly, et al. An image is worth 16x16 words: Transformers for image recognition at scale. *arXiv preprint arXiv:2010.11929*, 2020.
- [50] Ashish Vaswani, Noam Shazeer, Niki Parmar, Jakob Uszkoreit, Llion Jones, Aidan N Gomez, Łukasz Kaiser, and Illia Polosukhin. Attention is all you need. *Advances in neural information processing systems*, 30, 2017.
- [51] Andrew Jaegle, Felix Gimeno, Andy Brock, Oriol Vinyals, Andrew Zisserman, and Joao Carreira. Perceiver: General perception with iterative attention. In *International conference on machine learning*, pages 4651–4664. PMLR, 2021.
- [52] Ruibin Xiong, Yunchang Yang, Di He, Kai Zheng, Shuxin Zheng, Chen Xing, Huishuai Zhang, Yanyan Lan, Liwei Wang, and Tieyan Liu. On layer normalization in the transformer architecture. In *International Conference on Machine Learning*, pages 10524–10533. PMLR, 2020.
- [53] Zijie Li, Kazem Meidani, and Amir Barati Farimani. Transformer for partial differential equations’ operator learning. *arXiv preprint arXiv:2205.13671*, 2022.
- [54] Zhongkai Hao, Zhengyi Wang, Hang Su, Chengyang Ying, Yinpeng Dong, Songming Liu, Ze Cheng, Jian Song, and Jun Zhu. Gnot: A general neural operator transformer for operator learning. In *International Conference on Machine Learning*, pages 12556–12569. PMLR, 2023.
- [55] James Bradbury, Roy Frostig, Peter Hawkins, Matthew James Johnson, Chris Leary, Dougal Maclaurin, George Necula, Adam Paszke, Jake VanderPlas, Skye Wanderman-Milne, and Qiao Zhang. JAX: composable transformations of Python+NumPy programs, 2018.
- [56] Md Ashiqur Rahman, Zachary E Ross, and Kamyar Azizzadenesheli. U-no: U-shaped neural operators. *arXiv e-prints*, pages arXiv–2204, 2022.
- [57] Jayesh K Gupta and Johannes Brandstetter. Towards multi-spatiotemporal-scale generalized pde modeling. *arXiv preprint arXiv:2209.15616*, 2022.
- [58] Kimberly Stachenfeld, Drummond B Fielding, Dmitrii Kochkov, Miles Cranmer, Tobias Pfaff, Jonathan Godwin, Can Cui, Shirley Ho, Peter Battaglia, and Alvaro Sanchez-Gonzalez. Learned coarse models for efficient turbulence simulation. *arXiv preprint arXiv:2112.15275*, 2021.
- [59] Shuhao Cao. Choose a transformer: Fourier or galerkin. *Advances in neural information processing systems*, 34:24924–24940, 2021.
- [60] Zhongkai Hao, Chang Su, Songming Liu, Julius Berner, Chengyang Ying, Hang Su, Anima Anandkumar, Jian Song, and Jun Zhu. Dpot: Auto-regressive denoising operator transformer for large-scale pde pre-training. *arXiv preprint arXiv:2403.03542*, 2024.
- [61] Maarten V de Hoop, Daniel Zhengyu Huang, Elizabeth Qian, and Andrew M Stuart. The cost-accuracy trade-off in operator learning with neural networks. *arXiv preprint arXiv:2203.13181*, 2022.
- [62] Matthew Tancik, Pratul Srinivasan, Ben Mildenhall, Sara Fridovich-Keil, Nithin Raghavan, Utkarsh Singhal, Ravi Ramamoorthi, Jonathan Barron, and Ren Ng. Fourier features let networks learn high frequency functions in low dimensional domains. *Advances in neural information processing systems*, 33:7537–7547, 2020.

- [63] Ze Liu, Yutong Lin, Yue Cao, Han Hu, Yixuan Wei, Zheng Zhang, Stephen Lin, and Baining Guo. Swin transformer: Hierarchical vision transformer using shifted windows. In *Proceedings of the IEEE/CVF international conference on computer vision*, pages 10012–10022, 2021.
- [64] Sifan Wang, Hanwen Wang, and Paris Perdikaris. Learning the solution operator of parametric partial differential equations with physics-informed deepnets. *Science advances*, 7(40):eabi8605, 2021.
- [65] Sifan Wang, Shyam Sankaran, Hanwen Wang, and Paris Perdikaris. An expert’s guide to training physics-informed neural networks. *arXiv preprint arXiv:2308.08468*, 2023.
- [66] Benedikt Alkin, Andreas Fürst, Simon Schmid, Lukas Gruber, Markus Holzleitner, and Johannes Brandstetter. Universal physics transformers. *arXiv preprint arXiv:2402.12365*, 2024.
- [67] Yatian Pang, Wenxiao Wang, Francis EH Tay, Wei Liu, Yonghong Tian, and Li Yuan. Masked autoencoders for point cloud self-supervised learning. In *European conference on computer vision*, pages 604–621. Springer, 2022.
- [68] John D Hunter. Matplotlib: A 2d graphics environment. *Computing in science & engineering*, 9(03):90–95, 2007.
- [69] Charles R Harris, K Jarrod Millman, Stéfan J Van Der Walt, Ralf Gommers, Pauli Virtanen, David Cournapeau, Eric Wieser, Julian Taylor, Sebastian Berg, Nathaniel J Smith, et al. Array programming with numpy. *Nature*, 585(7825):357–362, 2020.
- [70] Diederik P Kingma and Jimmy Ba. Adam: A method for stochastic optimization. *arXiv preprint arXiv:1412.6980*, 2014.
- [71] Ilya Loshchilov and Frank Hutter. Decoupled weight decay regularization. *arXiv preprint arXiv:1711.05101*, 2017.
- [72] Elias M Stein and Rami Shakarchi. *Real analysis: measure theory, integration, and Hilbert spaces*. Princeton University Press, 2009.
- [73] Ilya Loshchilov and Frank Hutter. Sgdr: Stochastic gradient descent with warm restarts. *arXiv preprint arXiv:1608.03983*, 2016.

## A Nomenclature

Table 3 summarizes the main symbols and notation used in this work.

Table 3: Summary of the main symbols and notation used in this work.

Notation	Description
<b>Operator Learning</b>	
$\mathcal{X}$	The input function space
$\mathcal{Y}$	The output function space
$u \in \mathcal{X}$	Input function
$s \in \mathcal{Y}$	Output function
$y$	Query coordinate in the input domain of $s$
$\mathcal{G} : \mathcal{X} \rightarrow \mathcal{Y}$	The operator mapping between function spaces
$\mathcal{E} : \mathcal{X} \rightarrow \mathbb{R}^n$	Encoder mapping
$\mathcal{D} : \mathbb{R}^n \rightarrow \mathcal{Y}$	Decoder mapping
<b>Fourier Neural Operator</b>	
$\mathcal{F}, \mathcal{F}^{-1}$	Fourier transform and its inverse
$\mathcal{F}_n, \mathcal{F}_n^{-1}$	Discrete Fourier transform and its inverse truncated on the first $n$ modes
$K$	Linear transformation applied to the $n$ leading Fourier modes
$W$	Linear transformation (bias term) applied to the layer inputs
$k$	Fourier modes / wave numbers
$\sigma$	Activation function
<b>Continuous Vision Transformer</b>	
$\text{PE}_t$	Temporal positional embedding
$\text{PE}_s$	Spatial positional embedding
MSA	Multi-head self-attention
MHA	Multi-head attention
LN	Layer normalization
$P$	Patch size of Vision Transformer
$C$	Embedding dimension of Vision Transformer
$\mathbf{x} \in \mathbb{R}^{N_x \times N_y \times C}$	Latent grid features
$\epsilon$	Locality of interpolated latent grid features
<b>Partial Differential Equations</b>	
$\zeta$	Vorticity of shallow water equations
$\eta$	Height of shallow water equations
$\mathbf{u}$	Velocity field
$P$	Pressure field
$c$	Passive scalar (smoke)
$\nu$	Viscosity
<b>Hyperparameters</b>	
$B$	Batch size
$Q$	Number of query coordinates in each batch
$D$	Number of latent variables of interest
$T$	Number of previous time-steps
$H \times W$	Resolution of spatial discretization

## B The FNO layer as a conditioned neural field

**Proposition 1.** Suppose that a single layer of the Fourier Neural Operator (FNO) [4] is given by

$$s(y) = \sigma\left(Wu(y) + \mathcal{F}_n^{-1}(K\mathcal{F}_n(u))(y)\right). \quad (6)$$

Then the integral kernel term can be expressed as

$$\mathcal{F}_n^{-1}(K\mathcal{F}_n(u))(y) = \sum_{j=1}^n \Re(K\hat{u})_j \cos(2\pi\langle k_j, y \rangle) - \sum_{j=1}^n \Im(K\hat{u})_j \sin(2\pi\langle k_j, y \rangle), \quad (7)$$

*Proof.* Recall that the map  $\mathcal{F}_n : L^2 \rightarrow \mathbb{C}^n$  is the Fourier transform truncated to the first  $n$  modes and  $\mathcal{F}_n^{-1} : \mathbb{C}^n \rightarrow L^2$  is the left inverse of this operator,

$$\mathcal{F}_n^{-1}(z)(y) = \sum_{j=1}^n z_j e^{2\pi i \langle k_j, y \rangle} \quad (8)$$

Recall Euler’s formula,

$$e^{2\pi i \langle k, y \rangle} = \cos(2\pi\langle k, y \rangle) + i \sin(2\pi\langle k, y \rangle). \quad (9)$$

When the (complex) Fourier coefficients  $z_1, \dots, z_n$  come from a real valued signal, the imaginary components in the reconstruction equation 8 cancel and we are left with only real values. In this case, if we decompose each  $z_j$  into real and imaginary parts,  $z_j = \alpha_j + i\beta_j$ , then using equation 9 we rewrite equation 8 as

$$\mathcal{F}_n^{-1}(z)(y) = \sum_{j=1}^n \alpha_j \cos(2\pi\langle k_j, y \rangle) - \sum_{j=1}^n \beta_j \sin(2\pi\langle k_j, y \rangle). \quad (10)$$

This allows us to view the convolutional part of the FNO layer equation 2 as

$$\mathcal{F}_n^{-1}(K\mathcal{F}_n(u))(y) = \sum_{j=1}^n \Re(K\hat{u})_j \cos(2\pi\langle k_j, y \rangle) - \sum_{j=1}^n \Im(K\hat{u})_j \sin(2\pi\langle k_j, y \rangle), \quad (11)$$

where  $\hat{u} = \mathcal{F}_n u$  denotes the truncated Fourier transform of  $u$ , and  $\Re(z)$  and  $\Im(z)$  denote the real and imaginary parts of a complex vector  $z \in \mathbb{C}^n$ . □

## C Experimental Details

### C.1 Training and evaluation

**Training recipe.** We use a unified training recipe for all CViT experiments. We employ AdamW optimizer [70, 71] with a weight decay  $10^{-5}$ . Our learning rate schedule includes an initial linear warm-up phase of 5,000 steps, starting from zero and gradually increasing to  $10^{-3}$ , followed by an exponential decay at a rate of 0.9 for every 5,000 steps. The loss function is a one-step mean squared error (MSE) between the model predictions and the corresponding targets at the next time-step, evaluated at randomly sampled query coordinates:

$$\text{MSE} = \frac{1}{B} \frac{1}{Q} \frac{1}{D} \sum_{i=1}^B \sum_{j=1}^Q \sum_{k=1}^D \left| \hat{s}_i^{(k)}(\mathbf{y}_j) - s_i^{(k)}(\mathbf{y}_j) \right|_2^2, \quad (12)$$

where  $s_i^{(k)}(\mathbf{y}_j)$  denotes the  $k$ -th variable of the  $i$ -th sample in the training dataset, evaluated at a query coordinate  $\mathbf{y}_j$ , and  $\hat{s}$  denotes the corresponding model prediction. All models are trained for  $2 \times 10^5$  iterations with a batch size  $B = 64$ . Within each batch, we randomly sample  $Q = 1,024$  query coordinates from the grid and corresponding output labels.



**Training instabilities** We observe certain training instabilities in CViT models, where the loss function occasionally blows up, causing the model to collapse. To stabilize training, we clip all gradients at a maximum norm of 1. If a loss blowup is detected, we restart training from the last saved checkpoint.

**Evaluation.** After training, we obtain the predicted trajectory by performing an auto-regressive rollout on the test dataset. We evaluate model accuracy using the relative  $L^2$  norm, as commonly used in Li *et al.*[4]:

$$\text{Rel. } L^2 = \frac{1}{N_{\text{test}}} \frac{1}{D} \sum_{i=1}^{N_{\text{test}}} \sum_{k=1}^D \frac{\|\hat{s}_i^{(k)} - s_i^{(k)}\|_2}{\|s_i^{(j)}\|_2}, \quad (13)$$

where the norm is computed over the rollout prediction at all grid points, averaged over each variable of interest.

## C.2 Model Details

**CViT.** For the 1D advection equation, we create a tiny version of CViT to ensure the model size is comparable to other baselines. Specifically, we use a patch size of 4 to generate tokens. The encoder consists of 6 transformer layers with an embedding dimension of 256 and 16 attention heads. A single transformer decoder layer with 16 attention heads is used.

For the shallow water equation and Navier-Stokes equation, the CViT configurations are detailed in Table 4. While we use a patch size of  $8 \times 8$  by default, we use a smaller patch size of  $4 \times 4$  when training CViT-L for the Navier-Stokes problem. We find that using a smaller patch size better captures the small-scale features in flow motion, leading to improved accuracy.

Table 4: Details of Continuous Vision Transformer model variants.

Model	Encoder layers	Embedding dim	MLP width	Heads	# Params
CViT-S	5	384	384	6	13 M
CViT-B	10	512	512	8	30 M
CViT-L	15	768	1536	12	92 M

**DeepONet.** For the DeepONet, the branch network (encoder) is an MLP with 4 hidden layers of 512 neurons each. The trunk-net (decoder) also employs an MLP with 4 hidden layers of 512 neurons.

**NoMaD.** The encoder consists of 4 hidden layers with 512 neurons each, mapping the input to a latent representation of dimension 512. The decoder, also an MLP with 4 hidden layers of 512 neurons, takes the latent representation and maps it to the output function.

**Dilated ResNet.** Following the comprehensive experiments and ablation studies in PDEArena [57], we adopt the optimal Dilated ResNet configuration reported in their work. This model has 128 channels and employs group normalization. It consists of four residual blocks, each comprising seven dilated CNN layers with dilation rates of [1, 2, 4, 8, 4, 2, 1].

**U-Nets.** Based on comprehensive experiments and ablation studies in PDEArena [57], we select the two strongest U-Net variants reported in their work: **U-Net<sub>att</sub>** and **U-F2Net**. For both architectures, we use one embedding layer and one output layer with kernel sizes of  $3 \times 3$ . Besides, we use 64 channels and a channel multipliers of (1, 2, 2, 4) and incorporate residual connections in each downsampling and upsampling block. Pre-normalization and pre-activations are applied, along with GELU activations. For U-Net<sub>att</sub>, attention mechanisms are used in the middle blocks after downsampling. For U-F2Net, we replace the lower blocks in both the downsampling and upsampling paths of the U-Net architecture with Fourier blocks. Each Fourier block consists of 2 FNO layers with modes 16 and residual connections.

**UNO.** Following the comprehensive experiments and ablation studies in PDEArena [57], we adopt the optimal UNO of 128 channels.

**FNO.** For the 1D advection equation, our FNO model employs 3 Fourier neural blocks, each with 256 channels and 12 Fourier modes. The output is projected back to a 256-dimensional space before passing through a linear layer that produces the solution over the defined grid.

For the shallow water equation, we employ the best FNO model from comprehensive experiments and ablation studies in PDEArena [57]. Specifically, we use the FNO consisting of 4 FNO layers, each with 128 channels and 32 modes. Additionally, we use two embedding layers and two output layers with kernel sizes of  $1 \times 1$ , as suggested in Li *et al.*[4]. We use GeLU activation functions and no normalization scheme.

For the Navier-Stokes equation, we follow the problem setup in DPOT [60], which differs from the setup in PDEArena [57]. Therefore, we directly report the results from DPOT [60].

**FFNO / GK-T / OFormer / GNOT / DPOT.** We directly report the results from DPOT [60]. Detailed implementations can be found in their paper.

### C.3 Linear Advection Equation

We consider the one-dimensional linear advection equation

$$\frac{\partial u}{\partial t} + c \frac{\partial u}{\partial x} = 0, \quad x \in [0, 1],$$

with periodic boundary conditions  $u(0, t) = u(1, t)$  given an initial condition  $u(x, 0) = u_0(x)$  with the advection velocity  $c = 1$ . To generate discontinuous initial conditions, the initial condition  $u_0$  is assumed to be

$$u_0 = -1 + 2 \mathbb{1}_{\{\tilde{u}_0 \geq 0\}},$$

where  $\tilde{u}_0$  a centered Gaussian,

$$\tilde{u}_0 \sim \mathcal{N}(0, C) \text{ and } C = (-\Delta + \tau^2)^{-d}.$$

Here  $-\Delta$  denotes the Laplacian on  $D$  subject to periodic conditions on the space of spatial mean zero functions. Moreover,  $\tau$  denotes the inverse length scale of the random field and  $d$  determines the regularity of  $\tilde{u}_0$ . For this example, we set  $\tau = 3$  and  $d = 2$ .

**Dataset.** We make use of the datasets released by Hoop *et al.*[61]. This dataset consists of 40,000 samples of discretized initial conditions on a grid of  $N = 200$  points.

**Problem setup.** We follow the problem setup by Hoop *et al.*[61]. Our objective is to predict the solution profile at time  $t = 0.5$ . We compare the CViT model’s performance against several strong baseline neural operators: DeepONet [6], NoMaD [12] and Fourier Neural Operators [4]. For the training and evaluation, we considered a split of 20,000 samples used for training, 10,000 for validation, and 10,000 for testing.

**Training.** For all models, we use a batch size of 256 with a grid sampling size of 128, except for the FNO, which uses the full grid size of 200. The models are trained using the AdamW optimizer [71] with an exponential decay learning rate scheduler. The models are trained for 200,000 iterations, and the best model state is selected based on the validation set performance to avoid overfitting. The final performance is evaluated on the test set of 10,000 samples.

**Evaluation.** Due to the discontinuous nature of the problem, the relative L2 norm may not properly reflect the performance of the models. Instead, a more suitable metric for this task is the total variation [72], defined as

$$TV(f, g) = \int_{\Omega} ||\nabla f| - |\nabla g|| dx.$$

Table 5: Performance of neural operator architectures under the relative L2 and Total Variation metrics for the linear advection with discontinuous initial conditions benchmark.

Model	# Params	Rel. L2 error (% , ↓)			Total Variation error (↓)		
		Mean	Median	Worst-case	Mean	Median	Worst-case
FNO	4.98M	13.94	12.03	56.52	0.0406	0.0309	0.1910
DeepONet	2.20M	13.77	12.20	39.64	0.0572	0.0453	0.2300
NoMaD	2.21M	13.64	11.01	69.00	<b>0.0326</b>	<b>0.0245</b>	0.1732
CViT	3.03M	<b>11.70</b>	<b>10.68</b>	<b>35.44</b>	0.0334	0.0274	<b>0.1516</b>

The total variation quantifies the integrated difference between the magnitudes of the gradients of the predicted solution and the ground truth, providing a better indicator of a model’s ability to capture and preserve discontinuities in the solution.

Table 5 presents a summary of our results. We notice that the CViT model achieves the lowest mean, median and worst-case relative  $L^2$  errors, outperforming the other architectures on this metric. Furthermore, when considering the total variation metric, the CViT model exhibits competitive performance for the mean and median total variation values, and achieves the lowest prediction error the worst-case sample in the test dataset.

#### C.4 Shallow-Water equations

Let  $\mathbf{u}$  denote the velocity and  $\eta$  interface height which conceptually represents pressure. We define  $\zeta = \nabla \times \mathbf{u}$  and divergence  $\mathcal{D} = \nabla \cdot \mathbf{u}$ . The vorticity formulation is given by:

$$\begin{aligned} \frac{\partial \zeta}{\partial t} + \nabla \cdot (\mathbf{u}(\zeta + f)) &= 0, \\ \frac{\partial \mathcal{D}}{\partial t} - \nabla \times (\mathbf{u}(\zeta + f)) &= -\nabla^2 \left( \frac{1}{2} (u^2 + v^2) + g\eta \right), \\ \frac{\partial \eta}{\partial t} + \nabla \cdot (\mathbf{u}h) &= 0, \end{aligned}$$

subject to the periodic boundary conditions. Here  $f$  is Coriolis parameter and  $g = 9.81$  is the gravitational acceleration, and  $h$  is the dynamic layer thickness.

**Data generation.** The dataset is generated by PDEArena [57] using `SpeedyWeather.jl` on a regular grid with spatial resolution of  $192 \times 96$  ( $\Delta x = 1.875^\circ$ ,  $\Delta y = 3.75^\circ$ ), and temporal resolution of  $\Delta t = 48$  h. The resulting dataset contains 6,600 trajectories with a temporal spatial resolution  $11 \times 96 \times 192$ .

**Problem setup.** We follow the problem setup reported in PDEArena [57]. Our goal is to learn the operator that maps the vorticity and pressure fields from the previous 2 two time-steps to the next time-step. All models are trained with 5,600 trajectories and evaluated on the remain 1,000 trajectories. We report the relative  $L^2$  errors over 5-steps rollout predictions.

**Training.** For training CViT models, please refer to section C.1. For training other baselines in Table 1, we follow the recommended training procedure and hyper-parameters presented in PDEArena [57] Specifically, we use the AdamW optimizer with a learning rate of  $2 \times 10^{-4}$  and a weight decay of  $10^{-5}$ . Training is conducted for 50 epochs, minimizing the summed mean squared error. We use cosine annealing as the learning rate scheduler [73] with a linear warm-up phase of 5 epochs. An effective batch size of 32 is used for training.

#### C.5 Navier-Stokes equation

We consider the two-dimensional incompressible Navier-Stokes equations in the velocity-pressure formulation, coupled with a scalar field representing a transported particle concentration via the

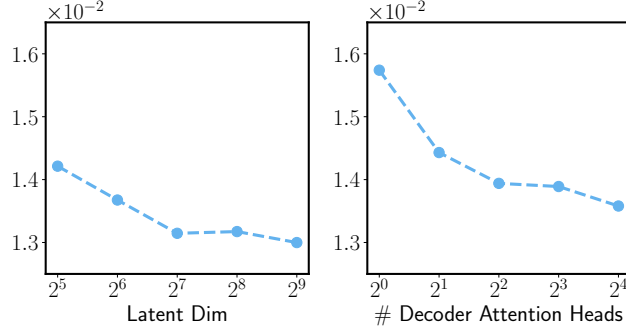


Figure 8: *Shallow water benchmark*. Ablation studies on the latent dimension of grid features and number of attention heads in decoder.

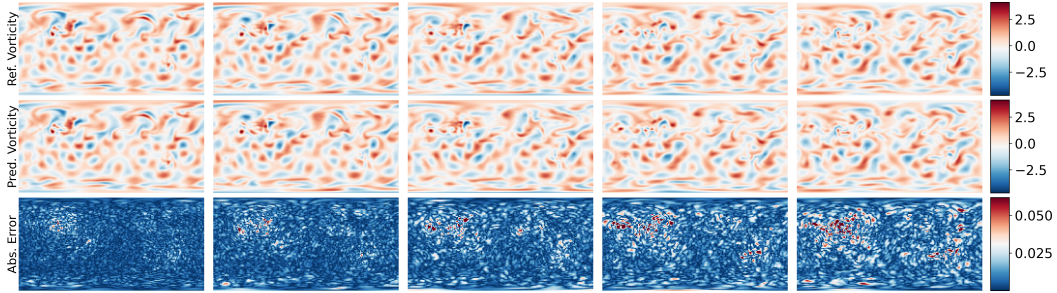


Figure 9: *Shallow water benchmark*. Representative CViT rollout prediction of the vorticity field, and point-wise error against the ground truth.

velocity field. The governing equations are given by:

$$\begin{aligned} \frac{\partial c}{\partial t} + \mathbf{u} \cdot \nabla c &= 0, \\ \frac{\partial \mathbf{u}}{\partial t} + \mathbf{u} \cdot \nabla \mathbf{u} + \nabla p - \nu \nabla^2 \mathbf{u} &= \mathbf{f}, \\ \nabla \cdot \mathbf{u} &= 0, \end{aligned}$$

where  $c$  is the scalar field,  $\mathbf{u}$  is the velocity field, and  $\nu$  is the kinematic viscosity. In addition, the velocity field is affected through an external buoyancy force term  $\mathbf{f}$  in the  $y$  direction, represented as  $\mathbf{f} = (0, f)^T$ .

**Data generation.** The 2D Navier-Stokes data is generated by PDEArena [57], which is obtained on a grid with a spatial resolution of  $128 \times 128$  ( $\Delta x = 0.25, \Delta y = 0.25$ ) and a temporal resolution of  $\Delta t = 1.5$  s. The simulation uses a viscosity parameter of  $\nu = 0.01$  and a buoyancy factor of

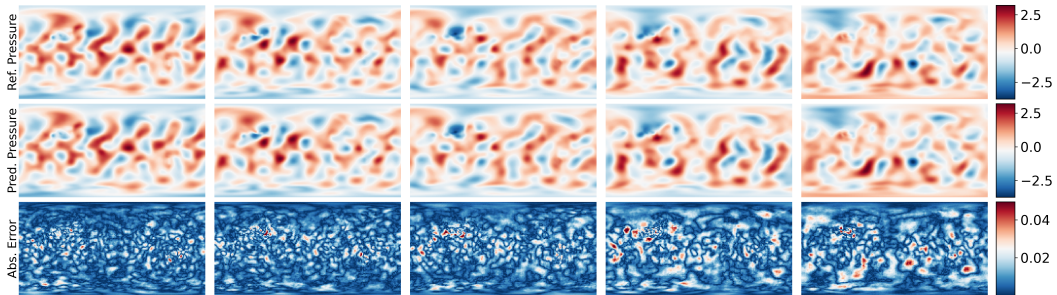


Figure 10: *Shallow water benchmark*. Representative CViT rollout prediction of the pressure field, and point-wise error against the ground truth.

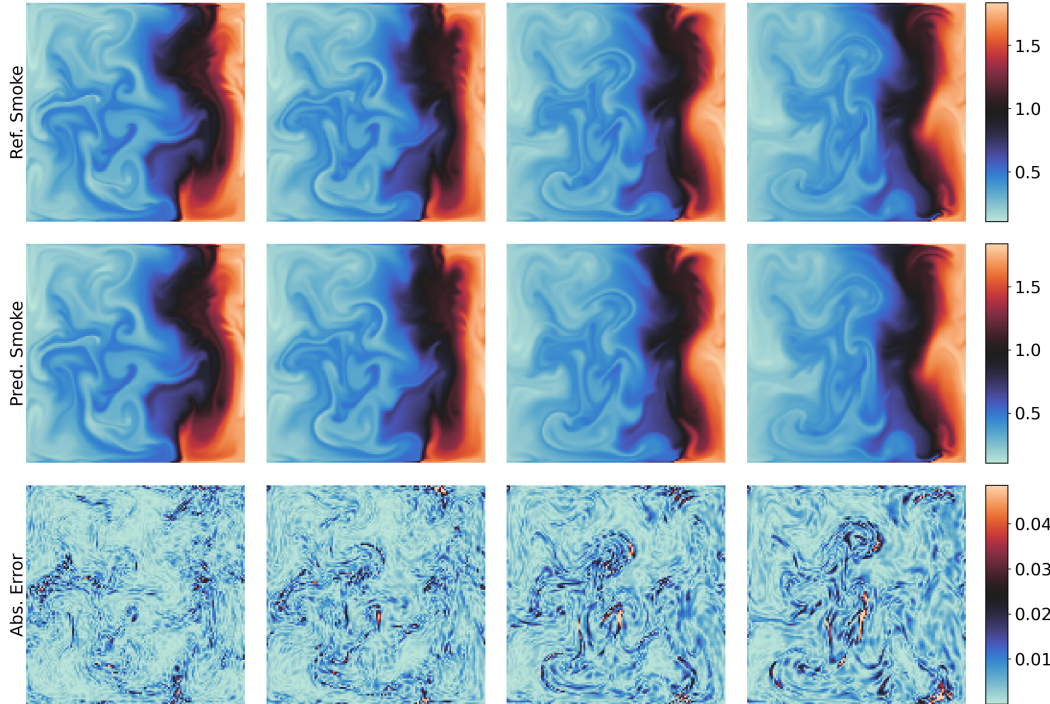


Figure 11: *Naiver-Stokes benchmark*. Representative CViT rollout prediction of the passive scalar field, and point-wise error against the ground truth.

$(0, 0.5)^T$ . The equation is solved on a closed domain with Dirichlet boundary conditions ( $v = 0$ ) for the velocity, and Neumann boundaries ( $\frac{\partial s}{\partial x} = 0$ ) for the scalar field. The simulation runs for 21 s, sampling every 1.5 s. Each trajectory contains scalar and vector fields at 14 different time frames, resulting in a dataset with 7,900 trajectories.

**Problem setup.** We follow the problem setup reported in Hao *et al.* [60]. We aim to learn the solution operator that maps the passive scalar and velocity fields from the previous 10 time-steps to the next time-step. The models are trained with 6,500 trajectories and tested on the remaining 1,300 trajectories. We report the resulting relative  $L^2$  errors over 4-steps rollout predictions.

**Evaluation.** We directly report the results as presented in DPOT [60]. For comprehensive details on the training procedures, hyper-parameters, please refer to their original paper.

## C.6 Computational Cost

All experiments were performed on a single Nvidia RTX A6000 GPU. Average training times varied between 5 hours and 60 hours, depending on the task, input resolution, model size, and patch size. The following table summarizes the training times for different models. We use a brief notation to indicate the model size and the input patch size: for instance, CViT-L/16 refers to the "Large" variant with a  $16 \times 16$  input patch size.



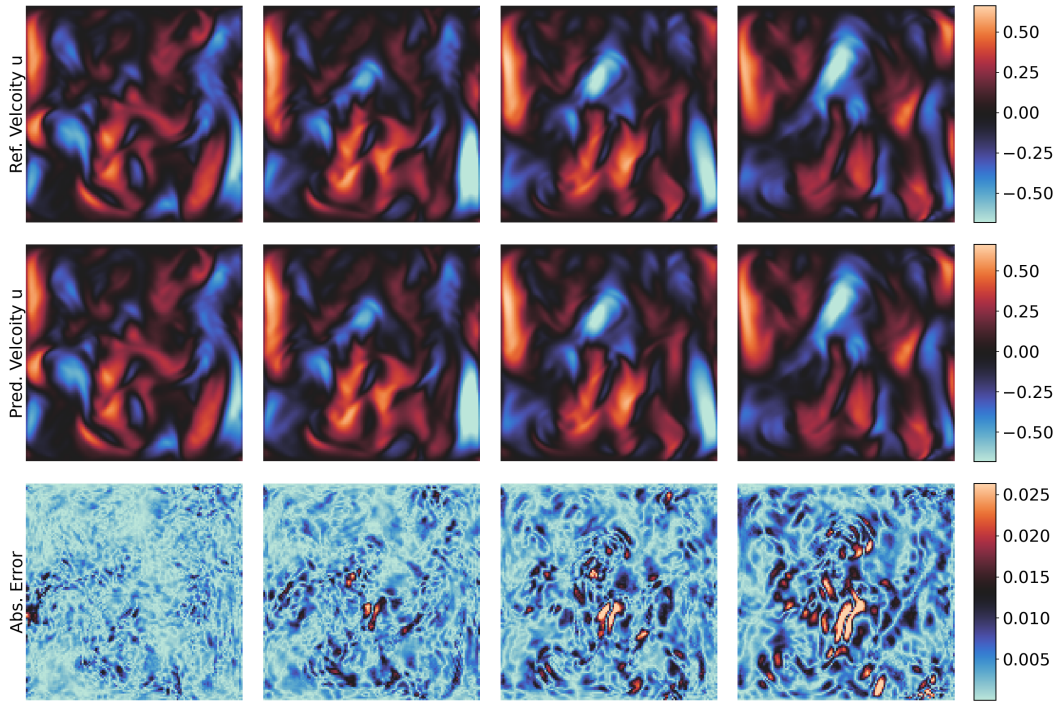


Figure 12: *Naiver-Stokes benchmark*. Representative CViT rollout prediction of the velocity field in  $x$  direction, and point-wise error against the ground truth.

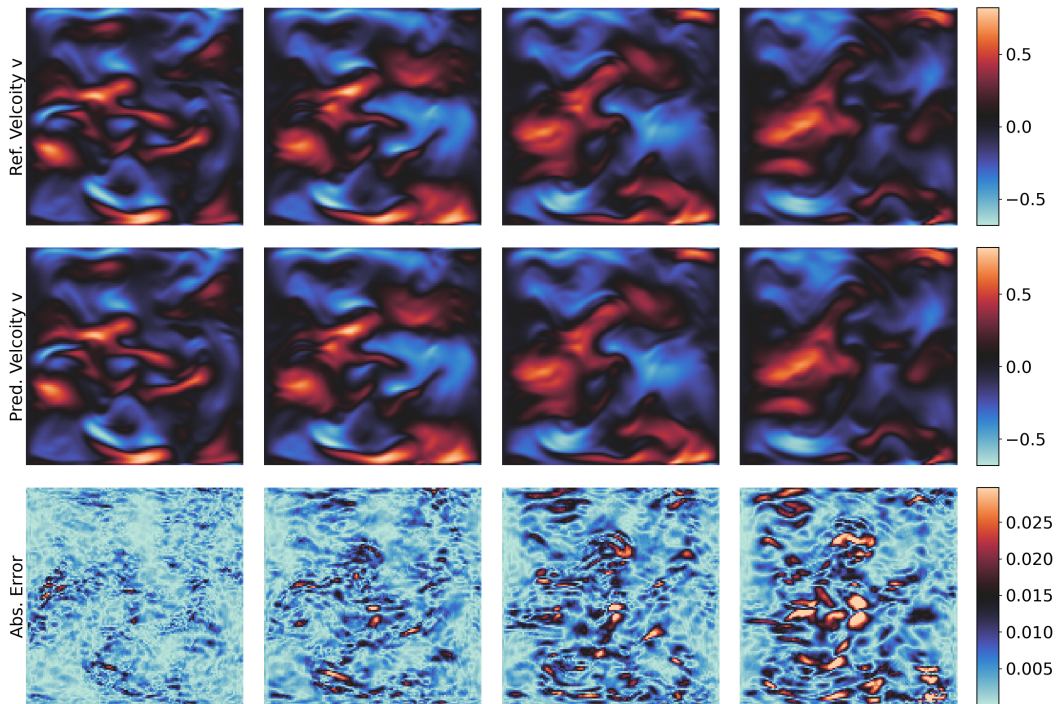


Figure 13: *Naiver-Stokes benchmark*. Representative CViT rollout prediction of the velocity field in  $y$  direction, and point-wise error against the ground truth.

Table 6: Training times (hours) on a single Nvidia RTX A6000 GPU for different models and patch sizes ( $8 \times 8$ ,  $16 \times 16$ ,  $32 \times 32$ ) on benchmarks of Shallow water equation and Navier-Stokes equation.

<b>Method</b>	<b>Shallow Water</b>	<b>Navier-Stokes</b>
CViT-S/8	15	9
CViT-B/8	25	14
CViT-L/8	57	28
CViT-L/16	17	10
CViT-L/32	9	6